

Deep learning-based neurodevelopmental assessment in preterm infants

Lexin Ren^{1†}, Jiamiao Lu^{1†}, Weichuan Zhang^{1*}, Benqing Wu^{2*},
 Tuo Wang^{3*}, Yi Liao^{1*}, Jiapan Guo^{4*}, Changming Sun^{5*},
 Liang Guo^{2*}

¹Image Computing Laboratory, Shaanxi University of Science and Technology, Xi'an, Shaanxi Province, China.

²Department of Neonatology, Shenzhen University of Advanced Technology General Hospital, Shenzhen, China.

³Department of Neurosurgery, The First Affiliated Hospital of Xi'an Jiaotong University, Xi'an, China.

⁴Department of Radiotherapy, University of Groningen, University Medical Center Groningen, Hanzeplein 1, 9713 GZ, Groningen, The Netherlands.

⁵CSIRO Data61, PO Box 76, Epping, NSW 1710, Australia.

*Corresponding author(s). E-mail(s): zwc2003@163.com;
wubenqing783@126.com; wt1972@tom.com; yi.liao@griffith.edu.au;
j.guo@umcg.nl; changming.sun@csiro.au; 419221185@qq.com;

Contributing authors: 251611018@sust.edu.cn; 241612058@sust.edu.cn;

†These authors contributed equally to this work.

Abstract

Preterm infants (born between 28 and 37 weeks of gestation) face elevated risks of neurodevelopmental delays, making early identification crucial for timely intervention. While deep learning-based volumetric segmentation of brain MRI scans offers a promising avenue for assessing neonatal neurodevelopment, achieving accurate segmentation of white matter (WM) and gray matter (GM) in preterm infants remains challenging due to their comparable signal intensities (isointense appearance) on MRI during early brain development. To address this, we propose a novel segmentation neural network, named Hierarchical Dense Attention Network. Our architecture incorporates a 3D spatial-channel attention mechanism combined with an attention-guided dense upsampling strategy

to enhance feature discrimination in low-contrast volumetric data. Quantitative experiments demonstrate that our method achieves superior segmentation performance compared to state-of-the-art baselines, effectively tackling the challenge of isointense tissue differentiation. Furthermore, application of our algorithm confirms that WM and GM volumes in preterm infants are significantly lower than those in term infants, providing additional imaging evidence of the neurodevelopmental delays associated with preterm birth. The code is available at: <https://github.com/ICL-SUST/HDAN>.

Keywords: Infant brain MRI segmentation, preterm infant tissue segmentation, neurodevelopment assessment

1 Introduction

Preterm infants, defined as neonates born between 28 and 37 weeks of gestation, account for approximately 11% of all deliveries worldwide [1]. Gestational age at birth is strongly correlated with neurological outcomes, and prematurity is recognized as a major risk factor for neurodevelopmental delay [2–5]. Infants born at lower gestational ages are particularly susceptible to cognitive and language impairments, as well as motor dysfunction [6, 7]. Given that current treatments for neurodevelopmental disorders are largely ameliorative rather than curative, the early identification of neuro-markers associated with neurodevelopmental delay is of critical importance [8, 9]. Such early detection would enable the development of targeted, preemptive intervention strategies aimed at improving long-term outcomes or potentially preventing these disorders altogether.

Infant brain MRI segmentation, which delineates brain tissues into mutually exclusive regions, is a fundamental step in the quantitative analysis of early brain development [10, 11]. By computing the volumetric measurements of different tissue types, researchers can quantitatively evaluate developmental trajectories during infancy [12]. Traditionally, brain segmentation has been performed manually by experienced clinicians [13]. However, this approach is labor-intensive, time-consuming, and susceptible to both intra- and inter-observer variability [14–17]. The reliance on highly skilled experts and substantial manual effort has hindered large-scale studies and slowed progress in early neurodevelopmental assessment.

With the recent integration of artificial intelligence (AI) techniques [18–62] into medical image analysis, automated MRI segmentation methods based on neural networks have emerged as a promising solution to overcome the inherent limitations of manual segmentation [63–66]. Recent studies [17, 66–68] have demonstrated that deep learning-based approaches can achieve comparable or even superior accuracy to expert annotations while significantly reducing analysis time, thereby facilitating large-scale population studies and enabling more efficient early identification of neurodevelopmental risk markers in preterm infants.

However, accurately segmenting white matter and gray matter in MRI scans of preterm infants remains a significant challenge. The first year of life is the most

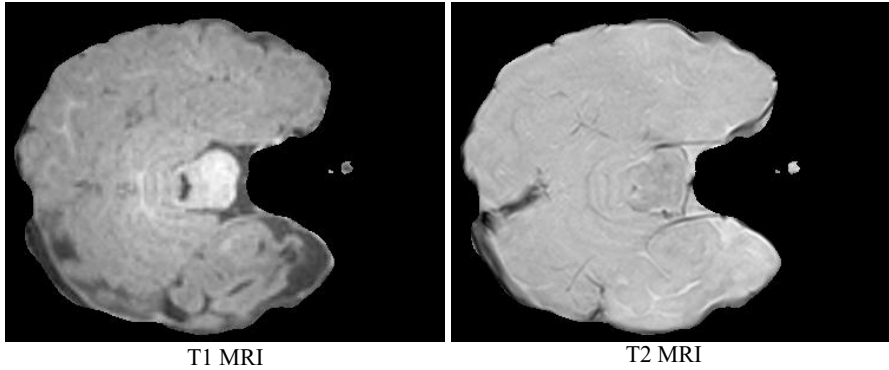


Fig. 1 MRI data of an preterm infant subject scanned at 9 months old (isointense phase). From left to right: T1 MRI and T2 MRI. It observed that the intensity level between white matter and gray matter is extremely similar, resulting in the low tissue contrast and thus making the segmentation a difficult challenge.

dynamic phase of postnatal human brain development, during which brain tissue grows rapidly, and cognitive as well as motor functions undergo substantial maturation [69, 70]. At this stage, white matter and gray matter display nearly identical intensity levels on both T1- and T2-weighted MRI images, leading to extremely low tissue contrast and making accurate segmentation particularly difficult [70, 71]. Therefore, this stage is also referred to as the isointense phase [72–74]. For term infants, the isointense phase typically emerges at approximately 6 to 8 months after birth [75, 76]; however, for preterm infants with delayed brain development, the timing of this phase remains uncertain, which undoubtedly further complicates the segmentation process. Fig. 1 shows examples of T1-weighted and T2-weighted MRI images acquired from a preterm infant at approximately 9 months of age. It can be observed that white matter and gray matter exhibit similar intensity levels, particularly in cortical regions, resulting in minimal tissue contrast and making tissue segmentation particularly challenging.

To the best of our knowledge, there are currently two main types of convolutional neural networks (CNNs) developed for volumetric infant brain segmentation. The first category consists of modified variants of 2D CNNs [77–80], which process individual slices or orthogonal planes (i.e., axial, coronal, and sagittal) to approximate three-dimensional spatial information.

Although these approaches have shown promising preliminary results, they cannot fully exploit the inherent 3D contextual information, thereby limiting their ability to achieve highly accurate object segmentation. The second category employs true 3D CNNs to segment objects directly from volumetric data, demonstrating compelling performance [66, 81–83]. However, efficiently training these deep 3D networks remains a challenge due to the high dimensionality of the data and the limited number of available training samples.

To bridge a critical gap in the early diagnosis of neurodevelopmental risks on brain MRI images among preterm infants, this paper introduces an automated 3D CNN-based model named HDAN for infant brain MRI volumetric segmentation. To ensure

robust feature extraction under limited training data, the proposed network adopts a standard Convolution-Batch Normalization-Activation design sequence to maintain training stability. Furthermore, by integrating the feature extractor with advanced 3D skip-connections, the network enhances feature representation capability, making it specifically suitable for preterm infant brain MRI images with low tissue contrast. In addition, we propose a 3D attention module to enlarge the intensity-level gap between white matter and gray matter, thereby improving the model’s recognition capability on low-contrast images.

The main contributions in this work can be summarized as follows:

- A novel automated 3D CNN-based segmentation model, HDAN, is proposed to address the challenging segmentation of low-contrast white matter and gray matter in MRI images.
- An Attention-Guided Dense Upsampling Block (AGDUB) is introduced to effectively recover fine-grained spatial details during the volumetric reconstruction phase, mitigating information loss typically caused by repeated down-sampling operations.
- To improve the feature representation capability, the proposed method integrates the inner feature extractor with 3D skip connections, making the model specifically suitable for feature extraction from preterm infant brain MRI images with low tissue contrast.
- To enhance the model’s recognition capability on low-contrast images, a 3D attention module is proposed to enlarge the intensity-level gap between gray and white matter on preterm infant brain MRI scans.
- Quantitative experiments on the benchmark dataset demonstrate that the proposed model not only obtains superior segmentation performance but also effectively delineates tissue boundaries in low-contrast infant brain MRI scans.

2 Related Work

2.1 3D Features for Volumetric Segmentation

Early brain MRI segmentation methods [77–79] primarily used 2D image processing. This approach limited their capacity to capture volumetric contextual information [84]. Utilizing inter-slice correlations improves the accuracy of 3D volumetric segmentation [85]. Both classical and recent studies [86–88] have shown that modeling 3D features or context significantly improves segmentation performance compared to traditional 2D slice-based methods. Based on these insights, many 3D convolutional architectures have been developed for biomedical volumetric segmentation. These include early lesion detection methods [89], encoder–decoder models such as 3D U-Net [81] and V-Net [82], as well as large-cohort multi-scale frameworks [90–92]. For example, the 3D U-Net [81] employs skip connections to enhance up-sampling. Dual-path CNNs [90] have also been developed for accurate brain lesion segmentation [93]. Although these models demonstrate clear advantages of 3D over 2D feature learning in volumetric brain image segmentation, most adopt the conventional 3D convolutional designs. However, optimizing these deep networks on limited medical datasets remains a challenging task that requires efficient architectural strategies.

2.2 3D-CNN for Volumetric Segmentation

Numerous studies [10, 68, 81, 82, 86, 94, 95] have explored the use of 3D CNNs for biomedical volumetric segmentation [88, 96, 97]. Hough-CNN [94] integrates a 3D CNN with a Hough voting mechanism for 3D segmentation. However, this method is not end-to-end and is mainly restricted to segmenting compact, blob-like structures [87, 88]. Kleesiek et al. [95] proposed an end-to-end 3D CNN for volumetric segmentation, but the network is shallow and cannot capture multiscale structures [98, 99]. To address this limitation, Moeskops et al. [63] introduced a multiscale CNN for infant brain tissue segmentation. Chen et al. [14] introduced residual learning to improve the training of fully convolutional networks (FCNs) for adult brain tissue segmentation. However, this approach ignores the information loss caused by pooling operations in FCNs, which can reduce segmentation accuracy. To overcome this, 3D-FCN [68] was proposed to enhance segmentation performance. However, it still struggles with small structures and precise localization due to coarse feature maps and resolution loss from repeated pooling [100]. These limitations motivate our design of an adaptive 3D attention mechanism that dynamically reweights volumetric features across both spatial and channel dimensions.

Although the aforementioned methods increase network capacity, they also present a common challenge: training becomes more difficult as network depth and complexity increase [88]. To address this, 3D-SkipDenseSeg [10] incorporates skip connections [101] within the fully convolutional DenseNet [102] architecture, allowing information to be concatenated from lower to higher dense blocks. These skip connections enable the network to leverage multi-level contextual information, thereby improving segmentation accuracy. However, stacked deconvolution layers result in a large number of learnable parameters, leading to increased memory consumption and training time [100].

More recently, Transformer-based frameworks have advanced medical image segmentation by enabling global contextual modeling beyond the local receptive fields of convolutional networks [97]. The self-configuring nnU-Net [98] established a strong 3D segmentation baseline, while UNETR [103] and Swin UNETR [104] introduced hierarchical attention mechanisms to effectively capture long-range dependencies in volumetric data. These developments complement convolutional designs and have motivated research into hybrid CNN-Transformer architectures.

3 The Proposed Method

3.1 Problem Definition

Given multi-modal MRI scans of infant brains, this study aims to perform voxel-wise segmentation that classifies each voxel into distinct tissue categories, including white matter (WM), gray matter (GM), and cerebrospinal fluid (CSF). Formally, let the input MRI volume be denoted as $I = \{I_{T1}, I_{T2}\} \in \mathbb{R}^{2 \times D \times H \times W}$, where the two channels correspond to the co-registered T1- and T2-weighted modalities. The segmentation network learns a mapping function $\mathcal{F} : I \rightarrow P$, where $P \in \mathbb{R}^{C \times D \times H \times W}$ is the predicted probability map with C tissue classes. The task is optimized by minimizing the cross-entropy loss between the predicted distribution and the ground truth labels.

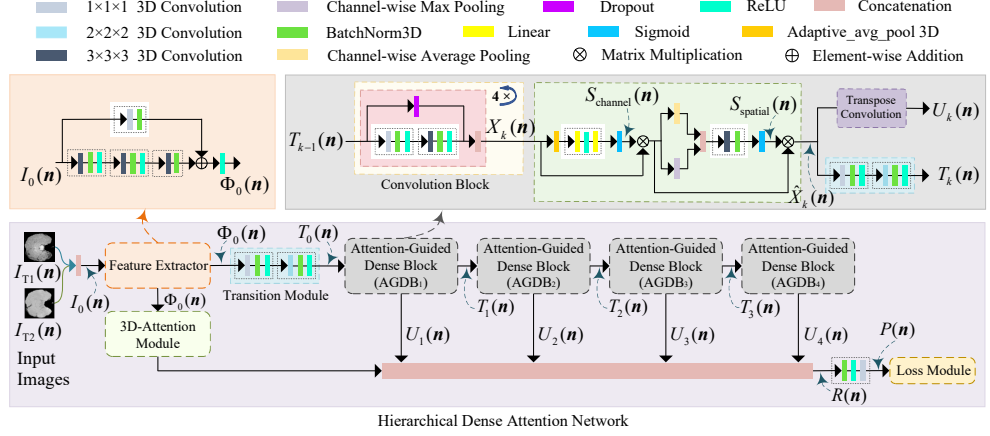


Fig. 2 The proposed architecture of **HDAN** (Hierarchical Dense Attention Network) for preterm infant brain volumetric segmentation. The framework consists of three main parts: **(a) Overall Architecture:** The multi-modal inputs are fused into $I_0(\mathbf{n})$ and processed by a hierarchical encoder-decoder structure. Multi-scale features are recursively extracted via four Attention-Guided Dense Blocks (AGDBs) and aggregated for dense prediction. **(b) Feature Extractor:** Detailed structure of the initial residual feature extraction module generating $\Phi_0(\mathbf{n})$. **(c) AGDB Internal Details:** Illustration of the internal information flow, highlighting the parallel generation of the next-stage feature $T_k(\mathbf{n})$ via the **Transition Module** and the upsampled feature $U_k(\mathbf{n})$ for global fusion.

3.2 Overall Framework

As illustrated in Fig. 2, the proposed Hierarchical Dense Attention Network (HDAN) adopts a recursive encoder-decoder strategy. Unlike conventional networks, HDAN introduces a parallel branching strategy within each encoding stage to simultaneously propagate deep semantic context (T_k) and fine-grained structural details (U_k). Let the spatial coordinate of a voxel be denoted as $\mathbf{n} = (x, y, z)$. The T1- and T2-weighted MRI volumes are channel-wise concatenated to form the unified input $I_0(\mathbf{n})$.

3.2.1 Encoding Path

The encoding process begins with a Feature Extractor $\mathcal{F}(\cdot)$, which maps the input $I_0(\mathbf{n})$ to the initial high-resolution feature maps $\Phi_0(\mathbf{n})$. To initiate the hierarchical representation, $\Phi_0(\mathbf{n})$ passes through an initial Transition Module $T_{\text{init}}(\cdot)$ to produce the base feature $T_0(\mathbf{n})$. Subsequently, the network recursively processes the features through four Attention-Guided Dense Blocks (AGDBs). Formally, for the k -th stage ($k = 1, \dots, 4$), each AGDB receives the transition feature $T_{k-1}(\mathbf{n})$ from the previous stage. Inside each AGDB, the feature undergoes dense convolution and 3D attention refinement to generate an intermediate refined feature $\hat{X}_k(\mathbf{n})$. Crucially, as shown in Fig. 2, this refined feature is split into two parallel branches:

- Hierarchical Transition Branch: $\hat{X}_k(\mathbf{n})$ is downsampled via a Transition Module $T_k(\cdot)$ to generate $T_k(\mathbf{n})$ as the input for the next stage.

- Deep Supervision Branch: $\hat{X}_k(\mathbf{n})$ is upsampled via a Transpose Convolution $\mathcal{U}_k(\cdot)$ to generate $U_k(\mathbf{n})$ for global fusion.

3.2.2 Global Fusion and Prediction

The decoder phase aggregates multi-scale features from all stages. The initial feature $\Phi_0(\mathbf{n})$ is refined by an independent attention module $\mathcal{A}_0(\cdot)$ to capture low-level texture cues. All hierarchical features are concatenated to construct the final dense representation $R(\mathbf{n})$:

$$\begin{aligned}
\Phi_0(\mathbf{n}) &= \mathcal{F}(I_0(\mathbf{n})), \\
T_0(\mathbf{n}) &= \mathcal{T}_{\text{init}}(\Phi_0(\mathbf{n})), \\
\hat{X}_k(\mathbf{n}) &= \mathcal{A}_k(\mathcal{C}_k(T_{k-1}(\mathbf{n}))), \quad k = 1, \dots, 4, \\
T_k(\mathbf{n}) &= \mathcal{T}_k(\hat{X}_k(\mathbf{n})), \\
U_k(\mathbf{n}) &= \mathcal{U}_k(\hat{X}_k(\mathbf{n})), \\
R(\mathbf{n}) &= \text{Concat}(\mathcal{A}_0(\Phi_0(\mathbf{n})), U_1(\mathbf{n}), \dots, U_4(\mathbf{n})), \\
P(\mathbf{n}) &= \text{Linear}(R(\mathbf{n})),
\end{aligned} \tag{1}$$

where \mathcal{F} , \mathcal{C}_k , \mathcal{A}_k , \mathcal{T}_k , and \mathcal{U}_k denote the Feature Extractor, Convolution Block, 3D Attention Module, Transition Module, and Transpose Convolution at stage k , respectively.

3.3 Attention-Guided Dense Block (AGDB)

The Attention-Guided Dense Block (AGDB) serves as the core processing unit within HDAN. Unlike conventional blocks that perform sequential operations, our AGDB integrates feature extraction, refinement, and distribution. As illustrated in Fig. 2, the AGDB comprises a Convolution Block for dense feature extraction and a 3D Attention Module for feature recalibration. Specifically, the input feature $T_{k-1}(\mathbf{n})$ first propagates through the Convolution Block to extract dense local features $X_k(\mathbf{n})$. Before any downsampling or upsampling occurs, $X_k(\mathbf{n})$ is modulated by the 3D Attention Module. This generates a spatially-refined feature $\hat{X}_k(\mathbf{n})$, which acts as a shared “clean” representation used by both the subsequent Transition Module and Transpose Convolution.

3.3.1 The Convolution Block

The Convolution Block aims to progressively refine high-level semantic representations. It is composed of four convolutional units operating in a residual manner. Each unit employs a pair of 3D convolutional layers ($1 \times 1 \times 1$ followed by $3 \times 3 \times 3$) to perform dimensional expansion and spatial aggregation. The dense connections facilitate gradient propagation and ensure comprehensive feature preservation for the attention mechanism.

3.3.2 The 3D Attention Module

The 3D Attention Module adaptively recalibrates volumetric feature responses across both channel and spatial domains, operating directly in 3D voxel space.

Channel Attention

This branch selectively enhances discriminative channels. Given a feature map F , a global average pooling operation aggregates channel-wise statistics, followed by two fully connected layers to generate channel weights M_c . The channel-reweighted feature is computed as $F_c = M_c \otimes F$.

Spatial Attention

Spatial attention emphasizes voxel dependencies. We apply both max- and average-pooling along the channel axis to form spatial descriptors. These are convolved to generate the spatial map M_s . The spatially refined feature is obtained as $F_s = M_s \otimes F_c$.

Unified Representation

The overall operation is formalized as:

$$F' = M_s(M_c(F)) \otimes F, \quad (2)$$

where \otimes denotes element-wise multiplication. This unified framework explicitly models voxel continuity, achieving structure-aware feature refinement that preserves local anatomical structures in low-contrast infant brain MRIs.

3.4 Other Network Components

3.4.1 Feature Extractor

The Feature Extractor serves as the initial encoding stage, transforming multi-modal MRI inputs into compact volumetric representations. As illustrated in Fig. 2, it follows the standard *Convolution–Normalization–Activation* design with residual connections to ensure training stability. Given the dual input modalities (T1 and T2), the number of input channels is set to 2. The output of this module, $\Phi_0(\mathbf{n})$, bifurcates into two paths: one feeds into the Initial Transition Module to start the hierarchical encoding (T_0), and the other passes through an independent 3D Attention Module to contribute to the final representation $R(\mathbf{n})$.

3.4.2 Transition Module

The Transition Module acts as an intermediate encoder stage that bridges low-level feature extraction and high-level semantic encoding. Each module contains two sequential 3D convolutional layers: a $1 \times 1 \times 1$ layer for channel projection and a $2 \times 2 \times 2$ layer for volumetric down-sampling. Through this compact design, the transition module filters redundant spatial details while transmitting discriminative volumetric representations (T_k) to the subsequent AGDB.

4 Experiments

4.1 Datasets

To comprehensively evaluate the segmentation performance and clinical applicability of the proposed HDAN, we utilized two distinct datasets: the iSeg-2019 challenge dataset for model benchmarking and the Pediatric Brain MRI dataset for neurodevelopmental assessment.

4.1.1 iSeg-2019 Dataset

The iSeg-2019 dataset [105] was employed to benchmark the proposed model against state-of-the-art methods. The dataset consists of 10 subjects (Subjects 1–10) designated for training and 13 subjects (Subjects 11–23) designated for testing. Each subject includes co-registered T1- and T2-weighted MRI scans with an isotropic resolution of $1 \times 1 \times 1 \text{ mm}^3$. The segmentation targets include white matter (WM), gray matter (GM), and cerebrospinal fluid (CSF), with ground-truth labels annotated by expert neuroradiologists.

In this study, we followed the standard partition provided in the dataset distribution: Subjects 1–10 were utilized for model training, and Subjects 11–23 were used for testing. It is important to note that while the ground-truth labels for the testing subjects were withheld during the original challenge phase, they have since been made available in post-challenge open-source repositories for offline research evaluation. Therefore, all quantitative metrics reported in this paper were computed locally using these ground-truth labels, ensuring a rigorous and reproducible assessment consistent with the dataset’s file structure.

4.1.2 Pediatric Brain MRI Dataset

The Pediatric Brain MRI [106] dataset consists of 833 infant brain MRI scans acquired using a Siemens Magnetom Skyra 3-T MRI scanner. In this study, to investigate neurodevelopmental patterns, we selected a subset of 54 samples, comprising 27 preterm infants and 27 full-term infants. This dataset serves as the basis for the clinical volumetric analysis presented in the subsequent discussion.

4.2 Evaluation Metrics

We quantitatively evaluate the segmentation performance using two standard metrics: the Dice Similarity Coefficient (Dice score) and the Modified Hausdorff Distance (MHD). The public evaluation tool [107] provided by the challenge organizers was used for computation. The Dice score measures the volumetric overlap between the predicted segmentation A and the ground truth G :

$$\text{DICE} = \frac{2|A \cap G|}{|A| + |G|}, \quad (3)$$

where $|A|$ and $|G|$ denote the number of foreground voxels in the prediction and ground truth, respectively. The DICE score ranges from 0 to 1, with a higher value

indicating superior segmentation accuracy. The MHD quantifies the shape similarity by measuring the average boundary discrepancy:

$$\text{MHD}(A, G) = \max \left(\frac{1}{|A|} \sum_{a \in A} \min_{g \in G} \|a - g\|, \frac{1}{|G|} \sum_{g \in G} \min_{a \in A} \|g - a\| \right), \quad (4)$$

where A and G here denote the set of points on the boundary of the predicted and ground-truth regions, respectively. A smaller MHD indicates smoother and more accurate boundary delineation.

4.3 Class Balancing Strategy

In infant brain segmentation, the number of voxels varies significantly across tissue categories (e.g., CSF vs. Background), leading to a class imbalance problem that may cause the model to bias towards the majority class. To mitigate this, we employ a Weighted Cross-Entropy Loss. Instead of treating all classes equally, we assign a specific weight w_c to each tissue category c , inversely proportional to its frequency in the training set. Formally, the weighted loss function is defined as:

$$\mathcal{L}_{\text{total}} = -\frac{1}{N} \sum_{i=1}^N \sum_{c=1}^C w_c \cdot \mathbb{I}(y^{(i)} = c) \cdot \ln P_c(\mathbf{n}_i), \quad (5)$$

where N is the total number of voxels, C is the number of classes, $y^{(i)}$ is the ground truth label, and $P_c(\mathbf{n}_i)$ is the predicted probability for class c . The weight w_c ensures that smaller structures (such as the detailed cortex in preterm infants) contribute sufficiently to the gradient updates, thereby improving the sensitivity of the model to fine-grained anatomical details.

4.4 Implementation Details

As is common in most medical imaging applications, the dataset available for model training is typically limited, whereas deep learning models generally require a large amount of data [108, 109]. Moreover, the proposed model usually processes full images to maintain a broad receptive field, which further exacerbates this challenge. To address these constraints and ensure reliable model training, we adopt a trade-off between receptive field size and dataset availability. Specifically, overlapping patches of size $64 \times 64 \times 64$ are extracted from both the original and manually segmented images. To increase the number of training samples, patches are slid across the entire volume with a defined step size, thereby generating a sufficient number of training samples. Network weights are initialized with PyTorch default initialization, which is equivalent to Kaiming uniform initialization for ReLU activations [110]. All bias terms are initialized to zero. A coarse linear search is then performed to select the initial learning rate and weight decay parameters, with the learning rate reduced by a factor of 10 at fixed intervals during training. The network is optimized using backpropagation [111]. The implementation is based on PyTorch, a popular deep learning framework. All experiments are implemented on an NVIDIA GeForce RTX 4090 GPU.

4.5 Quantitative Evaluation

In order to evaluate the superiority of the proposed model, we select 14 baseline methods for quantitative performance comparison. The baseline methods include FMRIB’s Automated Segmentation Tool (FAST) [112], Majority Voting (MV) [113], Random Forest (RF) [114], RF with Auto-Context Model (LINKS) [115], DeepMedic [90], 3D-UNet [81], CC-2D-FCN [64], DenseVoxNet [116], VoxResNet [14], CC-3D-FCN [68], HyperDenseNet [117], 3D-SkipDenseSeg [10], Swin-UNETR [104], and nnU-Net [98].

Table 1 Segmentation performance comparison for Dice score between baseline methods and ours on the iSeg-2019 dataset. A higher value is better. The best performance is highlighted in bold.

	White Matter	Gray Matter	Cerebrospinal Fluid
FAST [112]	0.453	0.393	0.557
MV [113]	0.562	0.710	0.713
RF [114]	0.821	0.839	0.859
LINKS [115]	0.839	0.857	0.885
DeepMedic [90]	0.844	0.859	0.917
3D-UNet [81]	0.836	0.862	0.897
CC-2D-FCN [64]	0.756	0.814	0.854
DenseVoxNet [116]	0.854	0.879	0.909
VoxResNet [14]	0.889	0.895	0.917
CC-3D-FCN [68]	0.919	0.903	0.934
HyperDenseNet [117]	0.889	0.889	0.926
3D-SkipDensSeg [10]	0.920	0.901	0.934
Swin-UNETR [104]	0.851	0.882	0.922
nnU-Net [98]	0.928	0.911	0.956
Ours	0.947*	0.937*	0.953

* indicates statistical significance ($p < 0.05$) compared to the runner-up method.

Table 1 reports the average similarity measured by the Dice score defined in Eq. (3), on the testing partition (Subjects 11–23) of the iSeg-2019 dataset. From Table 1, it is clear that the proposed HDAN outperforms the 12 baseline methods in terms of white matter, gray matter, and cerebrospinal fluid. The proposed method achieves average Dice scores of 0.947, 0.937, and 0.953 for white matter, gray matter, and cerebrospinal fluid, respectively.

Moreover, Table 2 reports the average MHD defined in Eq. (4) on the iSeg-2019 dataset. From Table 2, it clearly observed that the proposed model achieves the best segmentation performance in terms of the MHD metric.

Comparison with SOTA: As shown in Table 1, our method outperforms all CNN-based baselines. Furthermore, we compared our model with the self-configuring nnU-Net, a strong baseline in medical image segmentation. While nnU-Net achieves a slightly higher Dice score on the relatively distinct Cerebrospinal Fluid (CSF) region (0.956 vs. 0.953), our proposed method demonstrates superior performance on the most challenging tissues: White Matter (0.947 vs. 0.928) and Gray Matter (0.937 vs.

0.911). This significant improvement (approx. 2% on WM) validates that our proposed attention mechanisms effectively address the low-contrast “isointense” problem that standard U-Net architectures struggle with.

Table 2 Segmentation performance comparison for the MHD between baseline methods and ours on the iSeg-2019 dataset. The lower value is better. The best performance is highlighted in bold.

	White Matter	Gray Matter	Cerebrospinal Fluid
FAST [112]	1.714	1.012	1.838
MV [113]	1.771	1.196	1.963
RF [114]	0.695	0.594	0.475
LINKS [115]	0.569	0.489	0.439
DeepMedic [90]	0.519	0.499	0.475
3D-UNet [81]	0.602	0.463	0.483
CC-2D-FCN [64]	0.789	0.672	0.567
DenseVoxNet [116]	0.582	0.456	0.497
VoxResNet [14]	0.546	0.483	0.428
CC-3D-FCN [68]	0.259	0.179	0.285
HyperDenseNet [117]	0.335	0.289	0.314
3D-SkipDensSeg [10]	0.209	0.174	0.256
Swin-UNETR [104]	0.578	0.494	0.562
nnU-Net [98]	0.178	0.148	0.194
Ours	0.129	0.102	0.131

4.6 Qualitative Evaluation

To provide a visual comparison of tissue segmentation performance, three representative slices were randomly selected from a sample and segmented using the proposed method, CC-3D-FCN [68], and 3D-SkipDenseSeg [10]. The corresponding T1-weighted MRI images and ground truth labels are also presented for reference. As illustrated in Fig. 4, the regions with notable differences are highlighted by red rectangles. The segmentation produced by the proposed HDAN exhibits a higher consistency with the ground truth, particularly in the delineation of white matter, compared with the two baseline approaches.

4.7 Ablation Analysis

To validate the contribution of individual components in HDAN, we performed a stepwise ablation study on the iSeg-2019 dataset, with quantitative results summarized in Table 3.

4.7.1 Efficacy of the Backbone Network

We established a baseline model (denoted as “Baseline (Backbone)”) by removing the attention mechanisms and the dense upsampling strategy, retaining only the standard

Table 3 Ablation study of key components on the iSeg-2019 dataset. “Dense Up.” denotes Attention-Guided Dense Upsampling, “CA” denotes Channel Attention, and “SA” denotes Spatial Attention. The evaluation metrics include the average Dice score (\uparrow) and MHD (\downarrow) across all tissue classes.

Method	Dense Up.	CA	SA	Average Metric	
				Dice score \uparrow	MHD \downarrow
Baseline (Backbone)	\times	\times	\times	0.865	0.512
+ Dense Up. Only	✓	\times	\times	0.872	0.481
+ Dense Up. + SA	✓	\times	✓	0.885	0.315
+ Dense Up. + CA	✓	✓	\times	0.927	0.183
Proposed (All)	✓	✓	✓	0.946	0.121

residual encoder-decoder structure. As presented in Table 3, this baseline achieved a Dice score of 0.865 and an MHD of 0.512. These metrics indicate that while the deep residual backbone can capture the global semantic context of brain tissues, its ability to delineate precise boundaries is compromised. This limitation is intrinsic to standard convolutions when applied to the isointense phase of preterm infants, where the lack of explicit feature recalibration prevents the network from resolving the subtle intensity ambiguity at tissue interfaces.

4.7.2 Impact of Dense Upsampling

Incorporating the “Dense Up.” strategy alone (“+ Dense Up. Only”) yielded a moderate performance gain, improving the Dice score to 0.872 and reducing the MHD to 0.481. This result suggests that while dense connections facilitate gradient flow and feature reuse—thereby mitigating information loss during downsampling—they are insufficient to fully resolve boundary ambiguities. Without an attention mechanism to filter features, dense connections inevitably propagate both task-relevant semantics and redundant background noise, thereby limiting the upper bound of segmentation accuracy.

4.7.3 Critical Role of Attention Mechanisms

The integration of 3D attention modules proved to be the decisive factor in performance improvement. Introducing Spatial Attention (SA) refined the local structural details, increasing the Dice score to 0.885 while moderately reducing the MHD to 0.315. Furthermore, the addition of Channel Attention (CA) provided a substantial boost, reaching a Dice score of 0.927 and significantly lowering the MHD to 0.183. This dramatic reduction in boundary error demonstrates that explicit feature recalibration—which reweights informative channels and suppresses task-irrelevant responses—is essential for distinguishing isointense tissues from the complex background.

4.7.4 Synergistic Integration

The fully integrated “Proposed (All)” configuration achieved state-of-the-art performance, with a Dice score of **0.946** and an MHD of **0.121**. This confirms the synergistic effect between dense upsampling and attention mechanisms: the former ensures a robust flow of multi-scale information, while the latter dynamically filters this information to focus on anatomical validity. This combination enables HDAN to generate highly accurate segmentation maps even in the challenging isointense phase.

4.7.5 Visual Interpretability of Attention Mechanism

To elucidate why the proposed method significantly outperforms the baseline in boundary delineation (evidenced by the sharp decrease in MHD), we visualized the intermediate feature maps generated by the Spatial Attention module. As illustrated in Fig. 3, the attention mechanism functions as a robust feature selector. The visualization reveals that the module strongly suppresses the ventricular regions (Cerebrospinal Fluid, as shown in deep blue), effectively filtering out background noise. Conversely, the high-activation regions (highlighted in red and yellow hues) precisely track the geometry of the cortical ribbon. This empirical evidence corroborates that the HDAN does not merely memorize intensity values but explicitly learns the structural topology of the brain, thereby resolving the boundary ambiguity that hinders the baseline model.

4.8 Neurodevelopment Assessment in Preterm Infants

The primary goal of precise infant brain tissue segmentation is to enable reliable quantification of early neurodevelopment, particularly in preterm infants. White matter, a major component of the central nervous system, consists primarily of neuronal axons and their surrounding myelin sheaths. At birth, infant white matter remains immature, with incomplete myelination of axons. The first two postnatal years therefore represent a critical period of rapid white matter maturation [118]. Clinical investigations [119, 120] have frequently used white matter volume as a significant indicator of development progression. Accordingly, this study develops an efficient network-based automated framework to assess early brain development by quantifying both absolute and relative white matter volumes derived from voxel-level segmentation.

Recent neuroimaging evidence [74, 121] indicates that preterm infants generally exhibit smaller total brain volume and delayed cortical (gray matter) growth compared with term-born infants. To examine these developmental differences, brain MRI scans of 27 preterm and 27 age-matched term infants were retrospectively collected from the Pediatric Brain MRI dataset [106]. All scans were preprocessed under standardized clinical protocols to ensure consistent image quality across subjects. The proposed segmentation model was applied to delineate brain tissues, with particular emphasis on accurate white matter segmentation. Since ground truth masks were unavailable for this external dataset, we performed a rigorous visual inspection of the segmentation results on randomly selected samples. The proposed model demonstrated robust generalization capabilities, producing anatomically plausible tissue boundaries consistent with expert visual assessment, despite potential domain shifts between datasets. For

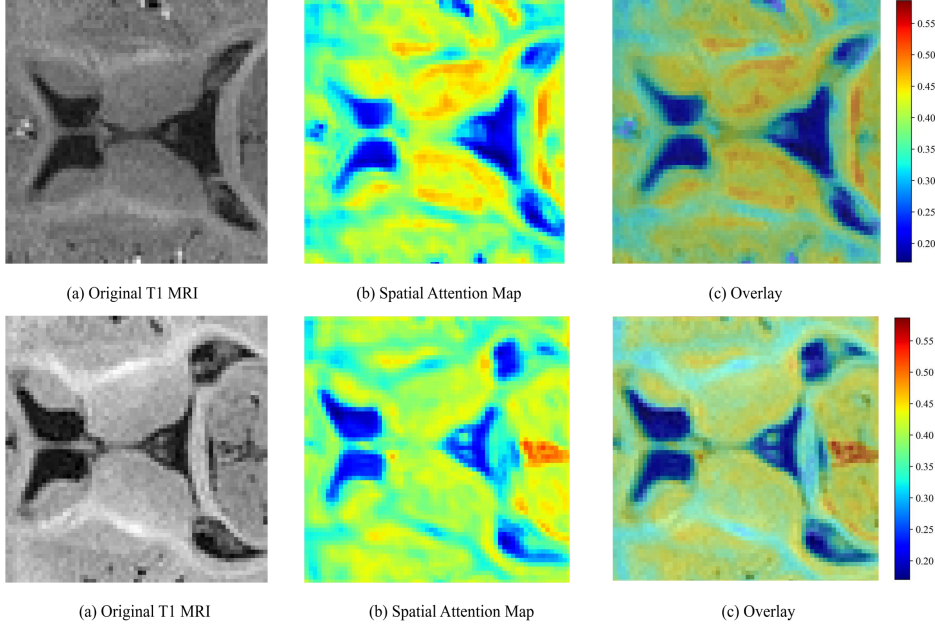


Fig. 3 Visualization of the Spatial Attention Map learned by the proposed HDAN. (a) The original T1-weighted MRI slice showing the low tissue contrast in the isointense phase. (b) The intermediate feature map extracted from the Spatial Attention module using the Jet colormap (Red: High attention; Blue: Low attention). (c) The overlay of the attention map on the original MRI. It can be clearly observed that the attention mechanism effectively suppresses the CSF within the ventricles (deep blue regions) while strongly activating along the tissue boundaries (indicated by red and yellow hues), demonstrating its capability to capture fine-grained structural details.

each subject, the voxel counts of white matter, gray matter, and cerebrospinal fluid were computed, from which both absolute and relative white matter measures (the white matter ratio) were derived.

The averaged results are summarized in Table 4. As presented in Table 4, the quantitative assessment reveals significant developmental differences. The mean white matter volume of preterm infants ($649, 152 \pm 42, 103 \text{ mm}^3$) was found to be significantly lower than that of term-born infants ($672, 657 \pm 38, 921 \text{ mm}^3$) with $p < 0.05$. This volumetric reduction is consistent with the incomplete myelination status expected in preterm development [74]. Moreover, the gray matter and total brain volumes (defined as the sum of WM and GM) were also markedly smaller ($p < 0.01$ and $p < 0.05$, respectively). Specifically, the total brain volume in the preterm group was $1,344, 275 \text{ mm}^3$, compared to $1,415, 334 \text{ mm}^3$ in the term group. Standardizing these metrics to physical volumes (mm^3) allows for direct comparison with clinical literature, confirming that our deep learning-based segmentation can reliably capture subtle volumetric deficits associated with prematurity.

Such trends are consistent with established neurodevelopmental patterns—indicating delayed cortical maturation and reduced overall brain growth in preterm infants rather than tissue-specific disproportion [118, 121].

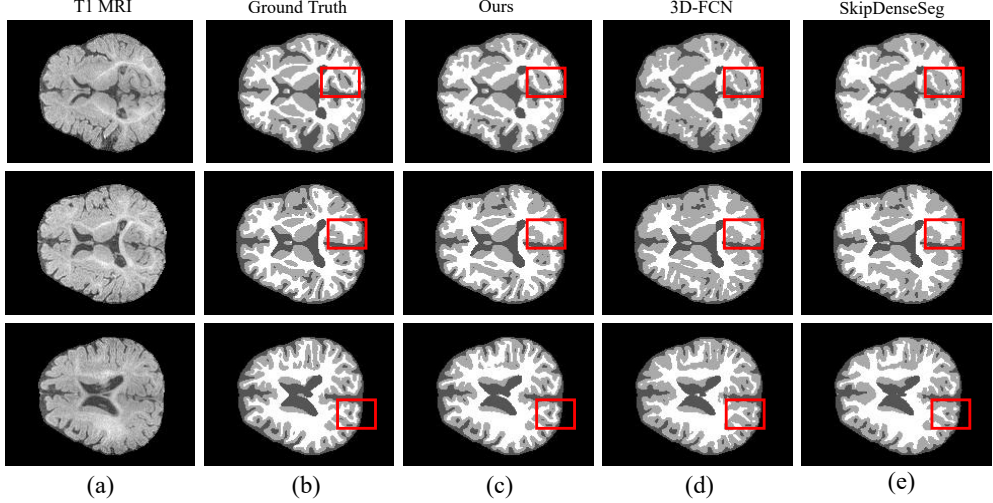


Fig. 4 Segmentation results produced by the proposed method and two baseline methods on different slices. (a) T1-weighted MRI; (b) ground truth label; (c) segmentation of the proposed method; (d) segmentation of 3D-FCN; (e) segmentation of SkipDenseSeg.

Table 4 Comparison of mean brain tissue volumes (mm^3) and white matter ratios (%) between preterm ($N = 18$) and term ($N = 27$) infants.

	WM	GM	CSF	Brain volume ¹	WM ratio ²
Preterm	649,152	695,123	474,353	1,344,275	48.15%
Term	672,657	742,677	425,307	1,415,334	47.42%
<i>p</i> -value	< 0.05	< 0.01	< 0.05	< 0.05	> 0.05

¹Defined as WM + GM (excluding CSF).

²Calculated as the mean of individual subject ratios, not the ratio of the means.

5 Conclusion

In this study, we proposed HDAN, a novel automatic 3D volumetric brain MRI segmentation framework for neurodevelopmental assessment in preterm infants. Unlike previous approaches constrained to 2D processing, our framework leverages a fully 3D convolutional architecture capable of handling multimodal MRI data. The standard Convolution-BatchNorm-ReLU design ensures training stability, while 3D skip connections enhance representational consistency. Furthermore, an integrated 3D attention mechanism improves feature discrimination and segmentation precision. Comprehensive quantitative and qualitative evaluations demonstrate the superior performance of the proposed model. When applied to preterm infant brain MRIs, the framework effectively identified characteristic developmental patterns—specifically, reduced

total brain and gray matter volumes with a relatively higher white matter proportion—consistent with previously reported indicators of delayed neurodevelopment in preterm populations [74, 118, 121].

Declarations

Funding. This work was supported by the Introduced Team Project (No. szgmtd2025001) at Shenzhen University of Advanced Technology General Hospital, featuring Professor Zhao Zhengyan's Pediatric Team from The Children's Hospital, Zhejiang University School of Medicine. Additional support was provided by the project titled “AI-based assessment of brain maturity and brain injury in preterm infants” (Grant No. Shen Ke Chuang Zi [2024] 47).

Competing interests. The authors declare no competing interests.

Ethics approval. This study was conducted using publicly available datasets and did not involve any new human participants or animal experiments performed by the authors. The datasets used in this study include the iSeg-2019 challenge dataset and the large dataset of infancy and early childhood brain MRIs. The original studies that collected these datasets received ethical approval from their respective institutional review boards, and all data were fully anonymized prior to public release. Therefore, no additional ethical approval was required for this study.

Informed consent. Informed consent was obtained from the legal guardians of all participants by the original data providers of the publicly available datasets.

Author contributions. Lexin Ren and Jiamiao Lu contributed equally to this work. All authors read and approved the final manuscript.

References

- [1] Ohuma, E.O., Moller, A.B., Bradley, E., *et al.*: National, regional, and global estimates of preterm birth in 2020, with trends from 2010: A systematic analysis. *Lancet* **402**, 1261–1271 (2023)
- [2] Marlow, N., Wolke, D., Bracewell, M.A., *et al.*: Neurologic and developmental disability at six years of age after extremely preterm birth. *New England Journal of Medicine* **352**, 9–19 (2005)
- [3] Glass, H.C., Costarino, A.T., Stayer, S.A., *et al.*: Outcomes for extremely premature infants. *Anesthesia & Analgesia* **120**, 1337–1351 (2015)
- [4] Mitha, A., Chen, R., Razaz, N., *et al.*: Neurological development in children born moderately or late preterm: A national cohort study. *The British Medical Journal* **384**, 075630 (2024)
- [5] Nivins, S., *et al.*: Gestational age and cognitive development in childhood. *The Journal of the American Medical Association Network Open* **8**, 254580 (2025)
- [6] Chen, Q., Zhang, K., Wang, M., *et al.*: A translational mouse model for investigation of the mechanism of preterm diffuse white matter injury. *Translational Pediatrics* **11**, 1074 (2022)
- [7] Loeffler, M.T., Daikeler, J., Wagner, L., *et al.*: Early expressive and receptive language development in preterm versus full-term children: A meta-analysis. *Pediatrics* **156**, 2024070477 (2025)
- [8] Zhao, Y., Liu, Y., Gao, X., *et al.*: Early biomarkers of neurodevelopmental disorders in preterm infants: Protocol for a longitudinal cohort study. *The British Medical Journal Open* **13**, 070230 (2023)
- [9] Vanderhasselt, T., Naeyaert, M., Buls, N., *et al.*: Synthetic magnetic resonance-based relaxometry and brain volume: Cutoff values for predicting neurocognitive outcomes in very preterm infants. *Pediatric Radiology* **54**, 1523–1531 (2024)
- [10] Bui, T.D., Shin, J., Moon, T.: Skip-connected 3D DenseNet for volumetric infant brain MRI segmentation. *Biomedical Signal Processing and Control* **54**, 101613 (2019)
- [11] Bethlehem, R.A.I., Seidlitz, J., Varikuti, D.P., *et al.*: Brain charts for the human lifespan. *Nature* **604**, 525–533 (2022)
- [12] Rossetti, L., Pascoe, L., Mainzer, R.M., *et al.*: Association between neonatal brain volume and school-age executive function in children born moderate-to-late preterm. *Pediatric Research* (2025)
- [13] Jain, R., Lee, F., Luo, N., *et al.*: A practical guide to manual and semi-automated

neurosurgical brain lesion segmentation. *Journal Of Neuroscience* **5**, 265–275 (2024)

[14] Chen, H., Dou, Q., Yu, L., *et al.*: VoxResNet: Deep voxelwise residual networks for brain segmentation from 3D MR images. *NeuroImage* **170**, 446–455 (2018)

[15] Makropoulos, A., Counsell, S.J., Rueckert, D.: A review on automatic fetal and neonatal brain MRI segmentation. *NeuroImage* **170**, 231–248 (2018)

[16] De Rosa, A.P., Benedetto, M., Tagliaferri, S., *et al.*: Consensus of algorithms for lesion segmentation in brain MRI studies of multiple sclerosis. *Scientific Reports* **14**, 21348 (2024)

[17] Wasserthal, J., *et al.*: TotalSegmentator MRI: robust sequence-independent segmentation of multiple anatomic structures in MRI. *Radiology* (2025). online ahead of print

[18] Jing, J., Liu, S., Liu, C., Gao, T., Zhang, W., Sun, C.: A novel decision mechanism for image edge detection. In: *International Conference on Intelligent Computing*, pp. 274–287 (2021). Springer

[19] Lu, J., Zhang, W., Zhao, Y., Sun, C.: Image local structure information learning for fine-grained visual classification. *Scientific Reports* **12**(1), 19205 (2022)

[20] Bao, J., Jing, J., Zhang, W., Liu, C., Gao, T.: A corner detection method based on adaptive multi-directional anisotropic diffusion. *Multimedia Tools and Applications* **81**(20), 28729–28754 (2022)

[21] Tang, Z., Wang, H., Yi, X., Zhang, Y., Kwong, S., Kuo, C.-C.J.: Joint graph attention and asymmetric convolutional neural network for deep image compression. *IEEE Transactions on Circuits and Systems for Video Technology* **33**(1), 421–433 (2022)

[22] Wang, J., Lu, J., Yang, J., Wang, M., Zhang, W.: An unbiased feature estimation network for few-shot fine-grained image classification. *Sensors* **24**(23), 7737 (2024)

[23] Lei, T., Song, W., Zhang, W., Du, X., Li, C., He, L., Nandi, A.K.: Semi-supervised 3-d medical image segmentation using multiconsistency learning with fuzzy perception-guided target selection. *IEEE Transactions on Radiation and Plasma Medical Sciences* **9**(4), 421–432 (2024)

[24] Liao, Y., Zhang, W., Gao, Y., Sun, C., Yu, X.: Asrsnet: Automatic salient region selection network for few-shot fine-grained image classification. In: *International Conference on Pattern Recognition and Artificial Intelligence*, pp. 627–638 (2022). Springer

- [25] Jing, J., Liu, S., Wang, G., Zhang, W., Sun, C.: Recent advances on image edge detection: A comprehensive review. *Neurocomputing* **503**, 259–271 (2022)
- [26] Pan, Z., Zhang, W., Yu, X., Zhang, M., Gao, Y.: Pseudo-set frequency refinement architecture for fine-grained few-shot class-incremental learning. *Pattern Recognition* **155**, 110686 (2024)
- [27] Jing, J., Gao, T., Zhang, W., Gao, Y., Sun, C.: Image feature information extraction for interest point detection: A comprehensive review. *IEEE Transactions on Pattern Analysis and Machine Intelligence* **45**(4), 4694–4712 (2022)
- [28] Zhang, W., Zhao, Y., Gao, Y., Sun, C.: Re-abstraction and perturbing support pair network for few-shot fine-grained image classification. *Pattern Recognition* **148**, 110158 (2024)
- [29] Shui, P.-L., Zhang, W.-C.: Corner detection and classification using anisotropic directional derivative representations. *IEEE Transactions on Image Processing* **22**(8), 3204–3218 (2013) <https://doi.org/10.1109/TIP.2013.2259834>
- [30] Shui, P.-L., Zhang, W.-C.: Noise-robust edge detector combining isotropic and anisotropic gaussian kernels. *Pattern Recognition* **45**(2), 806–820 (2012)
- [31] Zhang, W., Zhao, Y., Breckon, T.P., Chen, L.: Noise robust image edge detection based upon the automatic anisotropic gaussian kernels. *Pattern Recognition* **63**, 193–205 (2017)
- [32] Zhang, W.-C., Shui, P.-L.: Contour-based corner detection via angle difference of principal directions of anisotropic gaussian directional derivatives. *Pattern Recognition* **48**(9), 2785–2797 (2015)
- [33] Zhang, W., Sun, C.: Corner detection using multi-directional structure tensor with multiple scales. *International Journal of Computer Vision* **128**(2), 438–459 (2020)
- [34] Zhang, W., Sun, C., Breckon, T., Alshammari, N.: Discrete curvature representations for noise robust image corner detection. *IEEE Transactions on Image Processing* **28**(9), 4444–4459 (2019)
- [35] Zhang, W.-C., Wang, F.-P., Zhu, L., Zhou, Z.-F.: Corner detection using gabor filters. *IET Image Processing* **8**(11), 639–646 (2014)
- [36] Zhang, W., Sun, C.: Corner detection using second-order generalized gaussian directional derivative representations. *IEEE transactions on pattern analysis and machine intelligence* **43**(4), 1213–1224 (2019)
- [37] Li, Y., Zhang, W.: Traffic flow digital twin generation for highway scenario based on radar-camera paired fusion. *Scientific reports* **13**(1), 642 (2023)

[38] Qiu, B., Guo, J., Kraeima, J., Glas, H.H., Zhang, W., Borra, R.J., Witjes, M.J.H., Ooijen, P.M.: Recurrent convolutional neural networks for 3d mandible segmentation in computed tomography. *Journal of personalized medicine* **11**(6), 492 (2021)

[39] Liu, J., Yuan, F., Xue, C., Jia, Z., Cheng, E.: An efficient and robust underwater image compression scheme based on autoencoder. *IEEE Journal of Oceanic Engineering* **48**(3), 925–945 (2023)

[40] Jing, J., Liu, C., Zhang, W., Gao, Y., Sun, C.: Ecfrnet: Effective corner feature representations network for image corner detection. *Expert Systems with Applications* **211**, 118673 (2023)

[41] Wang, M., Zhang, W., Sun, C., Sowmya, A.: Corner detection based on shearlet transform and multi-directional structure tensor. *Pattern Recognition* **103**, 107299 (2020)

[42] Wang, J., Zhang, W.: A survey of corner detection methods. In: 2018 2nd International Conference on Electrical Engineering and Automation (ICEEA 2018), pp. 214–219 (2018). Atlantis Press

[43] Li, Y., Bi, Y., Zhang, W., Sun, C.: Multi-scale anisotropic gaussian kernels for image edge detection. *IEEE Access* **8**, 1803–1812 (2019)

[44] Liu, T., Xu, J., Lei, T., Wang, Y., Du, X., Zhang, W., Lv, Z., Gong, M.: Aekan: Exploring superpixel-based autoencoder kolmogorov-arnold network for unsupervised multimodal change detection. *IEEE Transactions on Geoscience and Remote Sensing* (2024)

[45] Ren, J., Li, C., An, Y., Zhang, W., Sun, C.: Few-shot fine-grained image classification: A comprehensive review. *AI* **5**(1), 405–425 (2024)

[46] Zhang, W., Liu, X., Xue, Z., Gao, Y., Sun, C.: Ndpnet: A novel non-linear data projection network for few-shot fine-grained image classification. *arXiv preprint arXiv:2106.06988* (2021)

[47] Li, Y., Feng, B., Zhang, W.: Mutual interference mitigation of millimeter-wave radar based on variational mode decomposition and signal reconstruction. *Remote Sensing* **15**(3), 557 (2023)

[48] Gao, T., Jing, J., Liu, C., Zhang, W., Gao, Y., Sun, C.: Fast corner detection using approximate form of second-order gaussian directional derivative. *IEEE Access* **8**, 194092–194104 (2020)

[49] Mital, N., Özyilkhan, E., Garjani, A., Gündüz, D.: Neural distributed image compression with cross-attention feature alignment. In: *Proceedings of the*

IEEE/CVF Winter Conference on Applications of Computer Vision, pp. 2498–2507 (2023)

- [50] Zhang, W., Sun, C., Gao, Y.: Image intensity variation information for interest point detection. *IEEE Transactions on Pattern Analysis and Machine Intelligence* **45**(8), 9883–9894 (2023)
- [51] Duan, W., Chang, Z., Jia, C., Wang, S., Ma, S., Song, L., Gao, W.: Learned image compression using cross-component attention mechanism. *IEEE Transactions on Image Processing* (2023)
- [52] Islam, M.A., Zhou, J., Zhang, W., Gao, Y.: Background-aware band selection for object tracking in hyperspectral videos. *IEEE Geoscience and Remote Sensing Letters* **20**, 1–5 (2023)
- [53] Liao, Y., Nikzad, N., Zhang, J., Zhang, W., Gao, Y.: Learning multiple receptive fields for few-shot image classification. In: 2025 31st International Conference on Mechatronics and Machine Vision in Practice (M2VIP), pp. 85–92 (2025). IEEE
- [54] Wang, M., Zheng, B., Wang, G., Yang, J., Lu, J., Zhang, W.: A principal component analysis-based feature optimization network for few-shot fine-grained image classification. *Mathematics* **13**(7), 1098 (2025)
- [55] Zheng, Z., Ren, H., Wu, Y., Zhang, W., Lu, H., Yang, Y., Shen, H.T.: Fully unsupervised domain-agnostic image retrieval. *IEEE Transactions on Circuits and Systems for Video Technology* **34**(6), 5077–5090 (2023)
- [56] Lu, J., Peng, G., Zhang, W., Sun, C.: Track-before-detect algorithm based on cost-reference particle filter bank for weak target detection. *IEEE Access* **11**, 121688–121701 (2023)
- [57] Liao, Y., Gao, Y., Zhang, W.: Dynamic accumulated attention map for interpreting evolution of decision-making in vision transformer. *Pattern Recognition* **165**, 111607 (2025)
- [58] Ren, J., An, Y., Lei, T., Yang, J., Zhang, W., Pan, Z., Liao, Y., Gao, Y., Sun, C., Zhang, W.: Adaptive feature selection-based feature reconstruction network for few-shot learning. *Pattern Recognition* (2025)
- [59] An, Y., Jing, J., Zhang, W.: Edge detection using multi-directional anisotropic gaussian directional derivative. *Signal, Image and Video Processing* **17**(7), 3767–3774 (2023)
- [60] Xie, D., Qiu, J., Sun, C., Zhang, W.: Second-order gaussian directional derivative representations for image high-resolution corner detection. *arXiv preprint arXiv:2601.08182* (2026)

- [61] Song, J., Sowmya, A., Zhang, W., Sun, C.: Efficient transformer with compressed attention for stereo image super-resolution. *Knowledge-Based Systems*, 114844 (2025)
- [62] Wang, W., Wang, M., Wang, H., Guo, W., Guo, J., Sun, C., Ma, L., Zhang, W.: Feature complementation architecture for visual place recognition. arXiv preprint arXiv:2506.12401 (2025)
- [63] Moeskops, P., Viergever, M.A., Mendrik, A.M., *et al.*: Automatic segmentation of MR brain images with a convolutional neural network. *IEEE Transactions on Medical Imaging* **35**, 1252–1261 (2016)
- [64] Long, J., Shelhamer, E., Darrell, T.: Fully convolutional networks for semantic segmentation. In: *IEEE Conference on Computer Vision and Pattern Recognition*, pp. 3431–3440 (2015)
- [65] Richter, L., Fetit, A.E.: Accurate segmentation of neonatal brain MRI with deep learning. *Frontiers in Neuroinformatics* **16**, 1006532 (2022)
- [66] Kim, M.-J., Hong, E., Yum, M.-S., *et al.*: Deep learning-based, fully automated, pediatric brain segmentation. *Scientific Reports* **14**, 4344 (2024)
- [67] Ronneberger, O., Fischer, P., Brox, T.: U-Net: Convolutional networks for biomedical image segmentation. In: *Medical Image Computing and Computer Assisted Intervention Society*, pp. 234–241 (2015)
- [68] Nie, D., Wang, L., Adeli, E., *et al.*: 3-D fully convolutional networks for multimodal isointense infant brain image segmentation. *IEEE Transactions on Cybernetics* **49**, 1123–1136 (2018)
- [69] Knickmeyer, R.C., Gouttard, S., Kang, C., *et al.*: A structural MRI study of human brain development from birth to 2 years. *Journal of Neuroscience* **28**, 12176–12182 (2008)
- [70] Mhlanga, S.T., Viriri, S.: Deep learning techniques for isointense infant brain tissue segmentation: A systematic literature review. *Frontiers in Medicine* **10**, 1240360 (2023)
- [71] Weisenfeld, N.I., Warfield, S.K.: Automatic segmentation of newborn brain MRI. *NeuroImage* **47**, 564–572 (2009)
- [72] Barkovich, A.J., Kjos, B.O., Jackson Jr, D.E., *et al.*: Normal maturation of the neonatal and infant brain: MR imaging at 1.5 T. *Radiology* **166**, 173–180 (1988)
- [73] Dubois, J., Dehaene-Lambertz, G., Kulikova, S., *et al.*: The early development of brain white matter: A review of imaging studies in fetuses, newborns and infants. *Neuroscience* **276**, 48–71 (2014)

- [74] Makropoulos, A., Robinson, E.C., Schuh, A., *et al.*: The developing human connectome project: A minimal processing pipeline for neonatal cortical surface reconstruction. *NeuroImage* **173**, 88–112 (2018)
- [75] Mhlanga, S.T., Viriri, S.: Deep learning techniques for isointense infant brain tissue segmentation: A systematic literature review. *Frontiers in Medicine* **10**, 1240360 (2023)
- [76] Baljer, L., Zhang, Y., Bourke, N.J., *et al.*: Ultra-low-field paediatric MRI in low- and middle-income countries: Super-resolution using a multi-orientation U-Net. *Human Brain Mapping* **46**, 70112 (2024)
- [77] Prasoon, A., Petersen, K., Igel, C., *et al.*: Deep feature learning for knee cartilage segmentation using a triplanar convolutional neural network. In: *Medical Image Computing and Computer Assisted Intervention Society*, pp. 246–253 (2013)
- [78] Liang-Chieh, C., Papandreou, G., Kokkinos, I., *et al.*: Semantic image segmentation with deep convolutional nets and fully connected CRFs. In: *International Conference on Learning Representations* (2015)
- [79] Zhang, W., Li, R., Deng, H., *et al.*: Deep convolutional neural networks for multi-modality isointense infant brain image segmentation. *NeuroImage* **108**, 214–224 (2015)
- [80] Wu, L., Wang, S., Liu, J., *et al.*: A survey of MRI-based brain tissue segmentation using deep learning. *Complex & Intelligent Systems* **11**, 64 (2025)
- [81] Cicek, O., Abdulkadir, A., Lienkamp, S.S., *et al.*: 3D U-Net: learning dense volumetric segmentation from sparse annotation. In: *Medical Image Computing and Computer Assisted Intervention Society*, pp. 424–432 (2016)
- [82] Milletari, F., Navab, N., Ahmadi, S.-A.: V-Net: Fully convolutional neural networks for volumetric medical image segmentation. In: *International Conference on 3D Vision*, pp. 565–571 (2016)
- [83] Chen, L., Wu, Z., Zhao, F., *et al.*: An attention-based context-informed deep framework for infant brain subcortical segmentation. *NeuroImage* **269**, 119931 (2023)
- [84] Avbersek, L.K., Repovs, G.: Deep learning in neuroimaging data analysis: Applications, challenges, and solutions. *Frontiers in Neuroimaging* **1**, 981642 (2022)
- [85] Zhang, Y., Liao, Q., Ding, L., *et al.*: Bridging 2D and 3D segmentation networks for computation-efficient volumetric medical image segmentation. *Computerized Medical Imaging And Graphics* **99**, 102088 (2022)

[86] Tran, D., Bourdev, L., Fergus, R., *et al.*: Learning spatiotemporal features with 3D convolutional networks. In: International Conference on Computer Vision, pp. 4489–4497 (2015)

[87] Zhou, H.Y., Guo, J., Zhang, Y., *et al.*: nnFormer: Volumetric medical image segmentation via a 3D transformer. *IEEE Transactions on Image Processing* **32**, 4036–4045 (2023)

[88] Xia, Q., Zheng, H., Zou, H., *et al.*: A comprehensive review of deep learning for medical image segmentation. *Neurocomputing* **613**, 128740 (2025)

[89] Dou, Q., Chen, H., Yu, L., *et al.*: Automatic detection of cerebral microbleeds from MR images via 3D convolutional neural networks. *IEEE Transactions on Medical Imaging* **35**, 1182–1195 (2016)

[90] Kamnitsas, K., Ledig, C., Newcombe, V.F., *et al.*: Efficient multi-scale 3D CNN with fully connected CRF for accurate brain lesion segmentation. *Medical Image Analysis* **36**, 61–78 (2017)

[91] Dolz, J., Desrosiers, C., Ayed, I.B.: 3D fully convolutional networks for subcortical segmentation in MRI: A large-scale study. *NeuroImage* **170**, 456–470 (2018)

[92] Billot, B., Magdamo, C., Cheng, Y., *et al.*: Robust machine learning segmentation for large-scale analysis of heterogeneous clinical brain MRI datasets. *Proceedings of the National Academy of Sciences of the United States of America* **120**, 2216399120 (2023)

[93] Fang, L., Wang, X.: Brain tumor segmentation based on the dual-path network of multi-modal MRI images. *Pattern Recognition* **124**, 108434 (2022)

[94] Milletari, F., Ahmadi, S.-A., Kroll, C., *et al.*: Hough-CNN: Deep learning for segmentation of deep brain regions in MRI and ultrasound. *Computer Vision And Image Understanding* **164**, 92–102 (2017)

[95] Kleesiek, J., Urban, G., Hubert, A., *et al.*: Deep MRI brain extraction: A 3D convolutional neural network for skull stripping. *NeuroImage* **129**, 460–469 (2016)

[96] Hatamizadeh, A., Nath, V., Tang, Y., *et al.*: UNETR: Transformers for 3D medical image segmentation. *Winter Conference on Applications of Computer Vision*, 574–584 (2022)

[97] Zhou, Y., Chen, X., *et al.*: Brain tumor segmentation and missing modality recovery using multi-modal latent feature learning. *Pattern Recognition* **141**, 109665 (2023)

[98] Isensee, F., Jäger, P., Full, P.M., *et al.*: nnU-Net: A self-configuring method for deep learning-based biomedical image segmentation. *Nature Methods* **18**, 203–211 (2021)

[99] Niyas, S., Pawan, S.J., Kumar, M.A., *et al.*: Medical image segmentation with 3D convolutional neural networks: A survey. *Neurocomputing* **493**, 397–413 (2022)

[100] Lilhore, U.K., Sunder, R., Simaiya, S., *et al.*: AG-MS3D-CNN: An attention-guided multiscale 3D convolutional neural network for robust brain tumor segmentation. *Scientific Reports* **15**, 24306 (2025)

[101] He, K., Zhang, X., Ren, S., *et al.*: Deep residual learning for image recognition. *Conference on Computer Vision and Pattern Recognition*, 770–778 (2016)

[102] Huang, G., Liu, Z., Maaten, L., *et al.*: Densely connected convolutional networks. *Conference on Computer Vision and Pattern Recognition*, 4700–4708 (2017)

[103] Hatamizadeh, A., Nath, V., Tang, Y., *et al.*: UNETR: Transformers for 3D medical image segmentation. In: *Winter Conference on Applications of Computer Vision*, pp. 574–584 (2022)

[104] Hatamizadeh, A., Nath, V., Tang, Y., *et al.*: Swin UNETR: Swin transformers for semantic segmentation of brain tumors in MRI images. In: *International MICCAI Brainlesion Workshop*, pp. 272–284 (2022). Springer

[105] Sun, Y., Gao, K., Wu, Z., *et al.*: Multi-site infant brain segmentation algorithms: The iSeg-2019 challenge. *IEEE Transactions on Medical Imaging* **40**, 1363–1376 (2021)

[106] Consortium, P.B.M.: Pediatric Brain MRI Dataset for Developmental Analysis. Available from database (2019)

[107] Taha, A.A., Hanbury, A.: Metrics for evaluating 3D medical image segmentation: Analysis, selection, and tool. *BMC Medical Imaging* **15**, 29 (2015)

[108] Krizhevsky, A., Sutskever, I., Hinton, G.E.: ImageNet classification with deep convolutional neural networks. In: *Conference on Neural Information Processing Systems*, vol. 25 (2012)

[109] Glorot, X., Bengio, Y.: Understanding the difficulty of training deep feedforward neural networks. In: *International Conference on Artificial Intelligence and Statistics*, pp. 249–256 (2010)

[110] He, K., Zhang, X., Ren, S., *et al.*: Delving deep into rectifiers: Surpassing human-level performance on ImageNet classification. In: *International Conference on Computer Vision*, pp. 1026–1034 (2015)

[111] LeCun, Y., Bottou, L., Orr, G.B., *et al.*: Efficient backprop. In: *Neural Networks:*

Tricks of the Trade, pp. 9–50 (2002)

- [112] Zhang, Y., Brady, M., Smith, S.: Segmentation of brain MR images through a hidden markov random field model and the expectation-maximization algorithm. *IEEE Transactions on Medical Imaging* **20**, 45–57 (2002)
- [113] Avants, B.B., Epstein, C.L., Grossman, M., *et al.*: Symmetric diffeomorphic image registration with cross-correlation: Evaluating automated labeling of elderly and neurodegenerative brain. *Medical Image Analysis* **12**, 26–41 (2008)
- [114] Breiman, L.: Random forests. *Machine Learning* **45**, 5–32 (2001)
- [115] Wang, L., Gao, Y., Shi, F., *et al.*: Links: Learning-based multi-source integration framework for segmentation of infant brain images. *NeuroImage* **108**, 160–172 (2015)
- [116] Yu, L., Cheng, J.-Z., Dou, Q., *et al.*: Automatic 3D cardiovascular MR segmentation with densely-connected volumetric convnets. In: *International Conference on Medical Image Computing and Computer Assisted Intervention*, pp. 287–295 (2017)
- [117] Dolz, J., Gopinath, K., Yuan, J., *et al.*: HyperDense-Net: A hyper-densely connected CNN for multi-modal image segmentation. *IEEE Transactions on Medical Imaging* **38**, 1116–1126 (2018)
- [118] Hüppi, P., Warfield, R., Kikinis, R., *et al.*: Quantitative magnetic resonance imaging of brain development in premature and mature newborns. *Annals of Neurology* **43**, 224–235 (1998)
- [119] Gilmore, J.H., Lin, W., *et al.*: Early postnatal development of corpus callosum and corticospinal white matter assessed with quantitative diffusion tensor imaging. *NeuroImage* **40**, 568–581 (2008)
- [120] Ball, G., Beare, M.C., *et al.*: Development of cortical microstructure in the preterm human brain. *Proceedings of the National Academy of Sciences of the United States of America* **115**, 5154–5163 (2018)
- [121] O’Muircheartaigh, J., Robinson, S., Pietsch, J., *et al.*: Modelling brain development to detect white matter injury in term and preterm born neonates. *NeuroImage* **219**, 117021 (2020)